Progress In Electromagnetics Research C, Vol. 172, 46–57, 2026

PIER C

(Received 13 May 2026, Accepted 18 June 2026, Scheduled 29 July 2026)

A Data-Driven Framework for the Efficient Design of Dual-Notched UWB Antennas via Surrogate-Assisted Nutcracker Optimization

Huawei Zhuang[1,*], Zijian Zhang[1], Fei Wang[1], Haonan Tian[1], Xiaoyang Liu[1], and Fanmin Kong[2]

[1]*School of Information & Electrical Engineering, Shandong Jianzhu University, Jinan 250101, China*
[2]*School of Information Science and Engineering, Shandong University, Tsingtao 266237, China*

ABSTRACT: The design of ultra-wideband (UWB) band-notched antennas is highly sensitive to geometric dimensions. Consequently, traditional metaheuristic algorithms incur prohibitive computational costs from massive full-wave electromagnetic (EM) simulations. An efficient co-design framework, termed the Surrogate-Assisted Nutcracker Optimization Algorithm with Gaussian Process (SANOA-GP), is proposed. By leveraging a GP surrogate for epistemic uncertainty quantification with a lower confidence bound (LCB) prescreening strategy, SANOA-GP balances exploration and exploitation, overcoming high-dimensional multimodal traps. Moreover, intelligent early stopping is achieved through a performance-driven dual-termination criterion with a progressive reward mechanism. Sobol global sensitivity analysis is incorporated to quantitatively evaluate geometric influences, enhancing black-box interpretability and verifying the independent tunability of the dual notches. Measurement results confirm that the optimized antenna achieves precise and deep notches ($S_{11} > -5$ dB) at the 5G N79 and X-band frequencies. Remarkably, SANOA-GP converges with an average of only 69.3 full-wave EM simulations. Compared to surrogate-free algorithms, it reduces computational time by over 50% while maintaining high optimization accuracy and physical reliability. The proposed framework offers an efficient and reliable paradigm for the automated design of complex radio frequency (RF) and microwave components.

1. INTRODUCTION

Ultra-wideband (UWB) systems are widely used in short-range high-speed communications and radar detection [1]. The key advantages of these systems include high data rates, low power consumption, and low probability of interception [2, 3]. However, the UWB spectrum overlaps with existing narrowband systems (e.g., WiMAX, WLAN, Sub-6 GHz 5G N79 band, and X-band satellite communications), causing severe electromagnetic interference (EMI) [4]. To achieve system compatibility and suppress interference, the design of UWB antennas with band-notched characteristics has become a research focus in RF engineering [5].

Complex geometric topologies and high-dimensional design parameters are typically involved in the design of high-performance band-notched antennas [6]. Precise notch control and passband impedance matching require modifications to the antenna structure. Such modifications introduce elements, including slots, stubs, or resonant rings, to the radiator or ground plane [7]. Consequently, antenna performance is highly sensitive to variations in geometric parameters, generating numerous local optima across the design space [8]. To effectively obtain the global optimum, traditional metaheuristic algorithms, such as Differential Evolution (DE) [9] and Particle Swarm Optimization (PSO) [10], are widely employed. It takes several minutes to complete an EM simulation for each fitness evaluation of algorithms [11]. Furthermore, thousands of full-wave EM simulations are required before the surrogate-free metaheuristic algorithms can converge [12]. Therefore, the computational cost is extremely high.

To reduce computational costs, antenna design increasingly adopts machine learning-based surrogate models, such as artificial neural networks and support vector regression [13]. Surrogate models replace costly EM simulations and dramatically accelerate the evaluation process. However, for most machine learning methods, a large number of high-quality samples must be generated in advance for offline training to ensure accuracy. In UWB band-notched antennas, the S_{11} curve exhibits multiple resonant points and dramatic variations at the notch edges, which significantly increases the modeling difficulty [14]. Consequently, if excessive simulation resources are consumed to generate training datasets for model training, the efficiency benefits of surrogate models are often negated. Furthermore, once an offline model is trained, it cannot easily adjust the design objectives, resulting in wasted computational resources [15].

To overcome the aforementioned computational challenges, an efficient co-design framework, SANOA-GP, is proposed for UWB dual-notch antennas [16, 17]. Recent Surrogate-Assisted Evolutionary Algorithms (SAEAs) directly combine surrogate models with optimization engines. In contrast, the

* Corresponding author: Huawei Zhuang (zhuanghuawei@sdjzu.edu.cn).

key innovation of our work lies in the synergistic integration of epistemic uncertainty quantification and a performance-driven dual-termination mechanism. Specifically, the global search capability of the NOA and the small-sample learning property of the GP are combined to eliminate the need for massive offline training samples. The GP model provides not only a predictive mean but also epistemic uncertainty through analytical predictive variance [18]. The uncertainty quantification dynamically balances the exploitation of known optimal regions against the exploration of unknown parameter boundaries [19, 20]. Such a balance effectively overcomes multimodal traps in the high-dimensional parameter space.

The main contributions of the paper are summarized as follows:

1. A synergistic co-design framework based on the GP and SANOA is proposed. Guided by the lower confidence bound (LCB) prescreening strategy, the analytical predictive variance is fully exploited to actively guide the NOA engine. Efficient optimization is performed by the online surrogate model under small-sample conditions, thus eliminating the requirement for pre-generating large-scale offline datasets.

2. Sobol global sensitivity analysis is incorporated to quantitatively evaluate the influence of key geometric parameters on the resonant characteristics of the antenna. The analysis enhances the interpretability of the black-box optimization and elucidates the underlying physical mechanisms of EM coupling between complex structures.

3. An efficient early stopping mechanism is proposed that uses a progressive reward and a dual-termination criterion. The strategy fundamentally resolves the trade-off between global exploration capability and computational cost. By integrating a multi-objective weighted fitness function with a performance-driven dynamic termination strategy, the algorithm avoids redundant evaluations. The proposed framework achieves robust convergence with an average of approximately 70 physical evaluations.

The remainder of this paper is organized as follows. In Section 2, the foundational theories of the related algorithms, including GP regression, NOA, and Sobol analysis, are presented. In Section 3, the implementation and workflow of the SANOA co-design framework are described. Section 4 discusses the experimental setup, comparative analysis of the optimization process, and final antenna performance verification. Finally, the conclusions of this study are summarized in Section 5.

2. PROPOSED ALGORITHMIC FRAMEWORK

The mathematical foundations of the proposed co-design framework are presented systematically in this section. Specifically, Gaussian process regression (GPR) is introduced to construct a probabilistic surrogate model. Then, the NOA is used to solve non-convex and multimodal optimization problems. Finally, a Sobol sensitivity analysis is employed to quantify the global influence of the input variables. Based on these foundations, the complete operational workflow of the SANOA-GP co-design framework is constructed.

2.1. Theoretical Foundations

GPR is a non-parametric probabilistic model that infers black-box functions from limited observations, providing both a predictive mean and variance that quantifies epistemic uncertainty. This predictive variance offers a rigorous basis for balancing global exploration and local exploitation in subsequent optimization.

To leverage this capability, GPR is applied to model the response of the antenna. For a D-dimensional input $\mathbf{x} \in \mathbb{R}^D$, the latent objective function is modeled as $f(\mathbf{x}) \sim \mathcal{GP}(m(\mathbf{x}), k(\mathbf{x}, \mathbf{x}'))$. In UWB antenna design, the S_{11} spectral responses typically exhibit abrupt transitions and highly nonlinear characteristics. Therefore, to accurately capture these physical behaviors, a Matérn-5/2 kernel with automatic relevance determination (ARD) is selected as the covariance function $k(\mathbf{x}, \mathbf{x}')$:

$$k_{\nu=5/2}(\mathbf{x}, \mathbf{x}') = \sigma_f^2 \left(1 + \sqrt{5} r_{\text{ARD}} + \frac{5}{3} r_{\text{ARD}}^2\right) \exp(-\sqrt{5} r_{\text{ARD}}) \tag{1}$$

where the scaled distance $r_{\text{ARD}} = \sqrt{\sum_{d=1}^{D} \frac{(x_d - x_d')^2}{l_d^2}}$, with σ_f^2 being the signal variance and l_d representing the length-scale for the d-th feature.

Given a training dataset $\mathcal{D} = \{\mathbf{X}, \mathbf{y}\}$ and observation noise variance σ_n^2, the posterior at a test point $\mathbf{x}_*$ is a Gaussian distribution with the following predictive mean and variance:

$$\mu(\mathbf{x}_*) = \mathbf{k}_*^T (\mathbf{K} + \sigma_n^2 \mathbf{I})^{-1} \mathbf{y} \tag{2}$$

$$\sigma^2(\mathbf{x}_*) = \sigma_f^2 - \mathbf{k}_*^T (\mathbf{K} + \sigma_n^2 \mathbf{I})^{-1} \mathbf{k}_* \tag{3}$$

where $\mathbf{K}$ is the covariance matrix of the training data, and $\mathbf{k}_*$ is the covariance vector between the test point $\mathbf{x}_*$ and the training points $\mathbf{X}$. By using the predictive variance $\sigma^2(\mathbf{x}_*)$ to identify highly uncertain regions, the algorithm effectively mitigates the risk of premature convergence to local optima in the high-dimensional design space. To intuitively illustrate this probabilistic mechanism, a conceptual diagram of the GPR is presented in Fig. 1. In the figure, a 95% confidence interval (shaded area) visually quantifies the epistemic uncertainty to guide global exploration, while the predictive mean directs local exploitation.

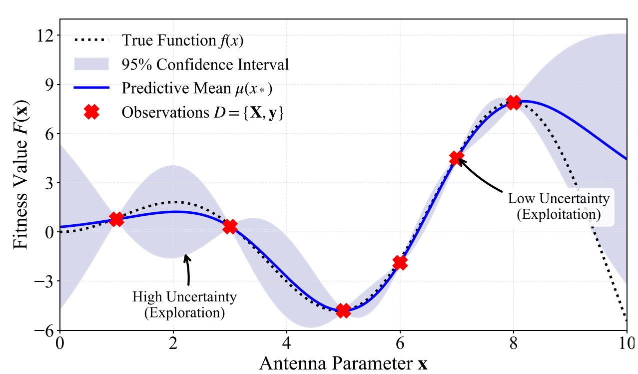

FIGURE 1. Diagram of Gaussian process regression: the predicted mean is represented by the solid line, and the 95% confidence interval is denoted by the shaded area.

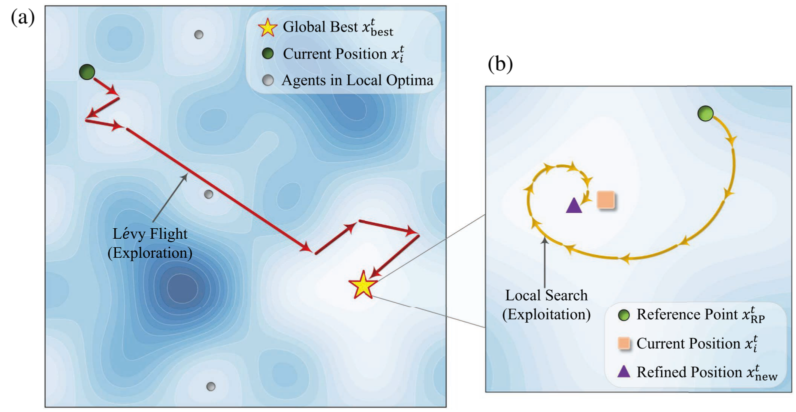

FIGURE 2. Schematic framework of the NOA dual-search mechanism. (a) illustrates global exploration via Lévy flights to escape local optima, whereas (b) depicts local exploitation around reference points.

NOA employs a dual-search mechanism to address high-dimensional, multimodal EM optimization problems (Fig. 2).

During global exploration, NOA uses Lévy flights to generate large random step sizes, effectively mitigating local-optima traps. The position update for the i-th individual $\mathbf{x}_i^t$ at generation t is given by

$$\mathbf{x}_{\text{new}}^t = \begin{cases} \mathbf{x}_i^t + \alpha \cdot \text{Lévy}(\beta) \cdot (\mathbf{x}_i^t - \mathbf{x}_{\text{best}}^t), & \text{if } r_1 < P_{a1} \\ \mathbf{x}_i^t + r_2 \cdot (\mathbf{x}_A^t - \mathbf{x}_B^t), & \text{otherwise} \end{cases} \tag{4}$$

where $\mathbf{x}_{\text{best}}^t$ is the global optimum of the current iteration; $\mathbf{x}_A^t$ and $\mathbf{x}_B^t$ are two randomly selected individuals; $r_1, r_2 \in [0, 1]$ are uniform random numbers; and P_{a1} is a probability threshold. Parameter α scales the step size, whereas β controls the tail heaviness of the Lévy distribution, thereby influencing the probability of generating large perturbations.

For local exploitation, NOA fine-tunes solutions around a historically optimal reference point $\mathbf{x}_{\text{RP}}^t$ within promising regions (Fig. 2(b)):

$$\mathbf{x}_{\text{new}}^t = \mathbf{x}_{\text{new}}^t + r_3 \cdot (\mathbf{x}_{\text{new}}^t - \mathbf{x}_{\text{RP}}^t) \cdot \exp(r_4 \pi) \tag{5}$$

where r_3 and r_4 govern the amplitudes of the local perturbations.

This seamless transition from coarse-grained global scanning to fine-grained local approximation significantly improves both the convergence speed and solution accuracy. Consequently, NOA serves as an ideal underlying solver for the surrogate-assisted framework in this study.

Sobol global sensitivity analysis is used to decompose the output variance and quantify the contributions of individual input variables and their interactions. Let $V(Y)$ be the total variance of the model output $Y = f(\mathbf{x})$. According to the Sobol decomposition,

$$V(Y) = \sum_{i=1}^{D} V_i + \sum_{1 \le i < j \le D} V_{ij} + \cdots + V_{1,2,\ldots,D} \tag{6}$$

where V_i is the variance attributed solely to the i-th variable, and V_{ij} is that arising from the interaction between the i-th and j-th variables. The first-order sensitivity index is then defined as:

$$S_i = \frac{V_i}{V(Y)} \tag{7}$$

which represents the main effect of X_i. The total-effect index $S_{\text{T}i}$ captures both the isolated contribution of X_i and all its interactions as follows:

$$S_{\text{T}i} = 1 - \frac{V_{\sim i}}{V(Y)} \tag{8}$$

where $V_{\sim i}$ is the variance contributed by all variables except X_i. By ranking $S_{\text{T}i}$, the key geometric parameters governing the antenna response are identified, providing a quantitative basis for interpreting the physical mechanisms of the dual-notch structure.

2.2. Co-Design Framework

Based on the aforementioned theoretical foundations, the co-design framework of SANOA-GP is constructed. This framework eliminates the reliance of traditional antenna optimization methods on computationally expensive full-wave simulations. A self-correcting, online, data-driven closed loop is established, in which low-fidelity virtual screening is efficiently integrated with high-fidelity EM validation. As shown in Fig. 3, three tightly coupled phases are integrated into the SANOA-GP framework: initial sampling and modeling, virtual evolutionary exploration, and closed-loop decision-making and updating.

The optimization process begins with Latin hypercube sampling (LHS) to generate a set of initial design vectors uniformly distributed across the multidimensional parameter space, effectively avoiding the sample clustering typical of purely random sampling. These samples are evaluated via full-wave EM simulations, and the resulting S_{11} responses, together with their corresponding geometric parameters, form the initial training database. The GPR model is then trained on this database to accurately fit the complex nonlinear EM responses and quantify epistemic uncertainty through predictive variance, establishing a robust mathematical foundation for the subsequent virtual search.

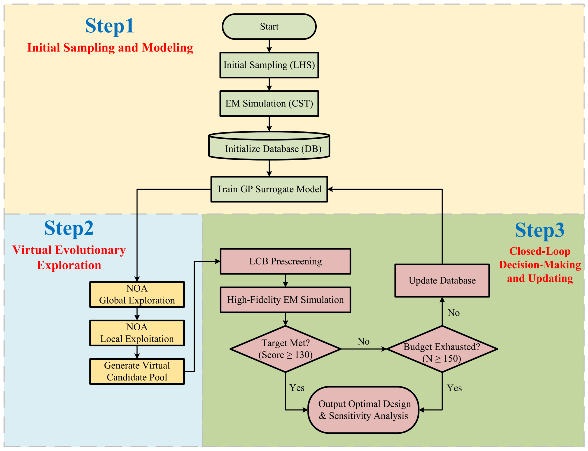

FIGURE 3. Flowchart of the proposed SANOA-GP co-design framework.

Next, the framework enters a virtual evolutionary exploration phase. The NOA performs population evolution entirely on the GP-predicted fitness landscape, eliminating the need for further EM simulations. Its dual-search mechanism, which combines Lévy flight-based global exploration and spatial-memory-based local search, guides individuals away from local optima and fine-tunes solutions within the identified promising regions. This computationally inexpensive virtual search rapidly traverses a vast design space, generating a pool of candidate solutions with high predicted performance.

However, surrogate fitting errors may misguide this virtual screening. Therefore, the LCB acquisition function prescreens candidates by integrating the predictive mean and variance, balancing exploitation and exploration. At each iteration, only the candidate with the optimal LCB value is submitted for high-fidelity EM validation.

Once a high-fidelity response is obtained, a dual-termination criterion is applied. If the actual fitness meets or exceeds the target threshold (Score $\geq$ 130), a performance-driven early-stopping mechanism is triggered, and the optimal design is immediately output, effectively conserving computational resources. Otherwise, provided that the cumulative number of EM simulations remains below the maximum budget of 150 simulations, a new high-fidelity data pair is added to the database, and the GP model is retrained. The online update continuously rectifies the surrogate model's epistemic bias, guiding the search to converge robustly to the true global optimum.

2.3. Complexity Analysis

The time complexity of the SANOA-GP framework is analyzed to quantify its efficiency advantage. In traditional metaheuristic algorithms directly coupled with full-wave EM simulators, the total time $T_{\text{Traditional}}$ is governed by the population size P, number of generations G, and duration of a single EM simulation T_{CST}:

$$T_{\text{Traditional}} \approx G \times P \times T_{\text{CST}}. \tag{9}$$

For complex antenna designs, the total number of physical evaluations $(G \times P)$ often reaches thousands, incurring a prohibitive computational burden.

In contrast, the SANOA-GP framework delegates the computationally intensive search to a surrogate model. Therefore, the total time depends almost entirely on the number of high-fidelity simulations, N_{real}, with $T_{\text{SANOA}} \approx N_{\text{real}} \times T_{\text{CST}}$. The overhead of GP training and virtual evolution is negligible because matrix-algebra operations are executed in milliseconds, whereas full-wave simulations require minutes. Guided by accurate surrogate predictions and the dual-termination criterion, N_{real} is several orders of magnitude smaller than the evaluation count of conventional algorithms ($N_{\text{real}} \ll G \times P$).

An order-of-magnitude reduction in computational time is achieved without compromising the design accuracy compared with conventional surrogate-free algorithms. Consequently, the proposed method provides an efficient paradigm for the automated design of high-dimensional, complex antennas.

3. ANTENNA PHYSICAL MODEL AND EXPERIMENTAL SETUP

3.1. Antenna Physical Model and Design Space

A compact UWB dual-notch antenna is selected as the benchmark design to evaluate the SANOA-GP algorithm's capability in solving high-dimensional, highly sensitive EM optimization problems. The antenna is printed on a standard FR-4 dielectric substrate with a relative permittivity of 4.4 and a thickness of 0.8 mm. The main radiator is formed by a semi-circular patch and a microstrip feedline. As depicted in Fig. 4, the geometric parameters of the inverted T-shaped stub and semi-circular slots on the radiating patch include the slot height L_1, total width W_1, inverted-T length T_1, arc width T_2, and top linewidth T_3. Similarly, the geometric parameters of the U-shaped parasitic stubs beside the microstrip feedline include the horizontal lengths U_1 and U_2, vertical length U_3, stub width c, and coupling gap d. The optimization bounds for these parameters are summarized in Table 1. Two angular variables, $R_1 \in [10°, 25°]$ and $R_2 \in [2°, 5°]$, are incorporated into the design space to precisely tune the curvature of the inverted U-shaped slot.

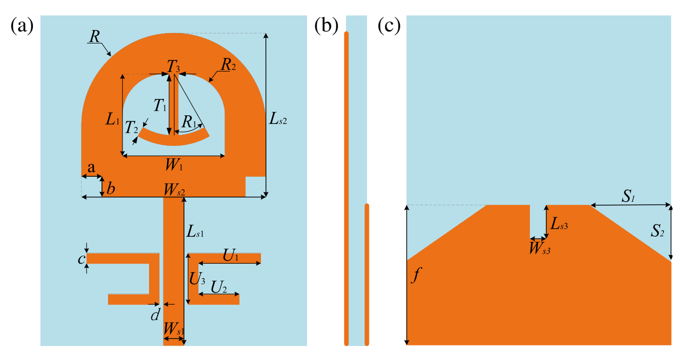

FIGURE 4. Antenna structure: (a) Front view of the antenna, (b) side view of the antenna, and (c) back view of the antenna.

The initial bounds of the 12 variables are estimated from transmission line theory. The resulting high-dimensional design vector $\mathbf{x} \in \mathbb{R}^{12}$ enables a thorough exploration of the global optimum while effectively avoiding local optima. Be-

TABLE 1. Design variables and their optimization bounds.

Parameter	Optimization Range (mm)
L_1	6–10
W_1	6–10
T_1	5–7
T_2	0.8–1.5
T_3	0.8–1.5
U_1	2.5–6
U_2	2.5–6
U_3	2.5–6
d	0.15–0.8
c	0.5–1.5

cause the mappings from the geometric parameters to the resonant frequencies are highly nonlinear, the notch center frequencies become extremely sensitive to minute perturbations in the key dimensions. Such sensitivity justifies the use of intelligent algorithms to navigate the multimodal landscape.

3.2. Objective Function and Early Stopping Criteria

In antenna optimization, the core objective is to achieve highly selective band-rejection at designated frequencies while preserving broadband impedance matching across the UWB passband. Accordingly, the design task is formulated as a maximization problem driven by a progressive reward mechanism. The entire operating spectrum is defined as $\Omega_{\text{all}} = [3.1\,\text{GHz}, 10.6\,\text{GHz}]$. The target dual-notch bands are specified as $\Omega_{\text{notch1}} = [4.4\,\text{GHz}, 5.0\,\text{GHz}]$ and $\Omega_{\text{notch2}} = [7.25\,\text{GHz}, 7.75\,\text{GHz}]$. The remaining frequencies are the passband Ω_{pass}.

A comprehensive fitness function $F(\mathbf{x})$ is constructed to ensure the efficient convergence of the SANOA-GP algorithm across the complex non-convex parameter space. It is defined as the weighted sum of a passband matching reward R_{pass}, a dual-notch suppression reward R_{notch}, and a numerical stability reward R_{stab}:

$$F(\mathbf{x}) = \omega_1 R_{\text{pass}}(\mathbf{x}) + \omega_2 \left(R_{\text{notch1}}(\mathbf{x}) + R_{\text{notch2}}(\mathbf{x})\right) + \omega_3 R_{\text{stab}}(\mathbf{x}) \tag{10}$$

where ω_1, ω_2, and ω_3 are the weight coefficients of the sub-objectives, used to balance the trade-offs among these competing objectives. The sub-objectives heavily reward solutions that satisfy the design specifications while providing smooth gradient guidance for underperforming candidates.

The impedance matching characteristics across the non-notched frequencies are evaluated by the passband matching reward R_{pass}. Let $\bar{S}_{\text{pass}}$ denote the mean reflection coefficient within the Ω_{pass} band. The mean value is deliberately used rather than the maximum value to provide a smoother optimization gradient. Furthermore, the passband target threshold is set to $T_{\text{pass}} = -10\,\text{dB}$. This reward term is formulated as the following piecewise function based on these parameters:

$$R_{\text{pass}}(\mathbf{x}) = \begin{cases} B_{\text{base}} + \gamma_1 (T_{\text{pass}} - \bar{S}_{\text{pass}}), & \text{if } \bar{S}_{\text{pass}} < T_{\text{pass}} \\ B_{\text{base}} \cdot \exp\left(-\frac{\bar{S}_{\text{pass}} - T_{\text{pass}}}{\tau}\right), & \text{otherwise} \end{cases} \tag{11}$$

where B_{base} is the base score, γ_1 the excess reward coefficient, and τ the decay constant. This mechanism provides positive, exponentially decaying gradient guidance for candidates that fail to meet the design specifications, helping them escape local optima. Conversely, for solutions satisfying the threshold, the linear term grants an excess reward to help the overall fitness swiftly reach the early stopping target.

A similar evaluation strategy is applied to the notch suppression reward R_{notch}. Let $S_{\text{max},k}$ denote the maximum reflection coefficient within the k-th notch band ($k = 1, 2$). Furthermore, the stopband target threshold is set to $T_{\text{stop}} = -5\,\text{dB}$. Based on these conditions, the reward function is formulated as follows:

$$R_{\text{notch},k}(\mathbf{x}) = \begin{cases} B_{\text{notch}} + \gamma_2 (S_{\text{max},k} - T_{\text{stop}}), \\ \text{if } S_{\text{max},k} > T_{\text{stop}} \\ B_{\text{notch}} \cdot \exp\left(-\dfrac{T_{\text{stop}} - S_{\text{max},k}}{\tau}\right), \\ \text{otherwise} \end{cases} \tag{12}$$

The weighted-sum fitness formulation strongly drives the algorithm to achieve high reflection characteristics ($S_{11} > -5\,\text{dB}$) within the notch bands, thereby ensuring a sufficient interference suppression depth.

Furthermore, a numerical stability reward term R_{stab} is introduced to eliminate physically spurious solutions characterized by non-physical, violent oscillations in the frequency response. Let $\text{std}(S_{11})$ denote the standard deviation of the S_{11} curve within the passband and δ the allowable fluctuation threshold. The stability term is defined as:

$$R_{\text{stab}}(\mathbf{x}) = \begin{cases} B_{\text{stab}}, & \text{if } \text{std}(S_{11}) < \delta \\ B_{\text{stab}} - \lambda \cdot (\text{std}(S_{11}) - \delta), & \text{otherwise} \end{cases} \tag{13}$$

A performance-driven dual-termination criterion is adopted to rigorously govern the optimization process and balance the computational cost and design accuracy. Once the comprehensive fitness score $F(\mathbf{x})$ of a candidate solution exceeds the predefined target threshold of 130, the optimization is terminated immediately.

In the weighted-sum fitness function, the exponential penalty terms in Eqs. (11)–(12) are not triggered if and only if the antenna simultaneously satisfies the passband matching baseline ($\bar{S}_{\text{pass}} \leq -10\,\text{dB}$), the dual-notch suppression baseline ($S_{\text{max},k} \geq -5\,\text{dB}$), and the numerical stability requirement. Each sub-reward function then guarantees its full base score, and their weighted sum yields exactly 130 points. The reverse-engineering of the fitness threshold from physical metrics gives the SANOA-GP framework strong generalizability. For other complex antenna or microwave component designs, designers need not rely on trial and error to set the target score. Instead, by substituting their specific S-parameter requirements into the progressive reward formulas, a new termination threshold can be dynamically calculated. The co-design framework can thus be efficiently applied to RF engineering problems with diverse specifications. If the target score remains unmet, the optimization continues until the maximum budget of 150 full-wave EM simulations is exhausted. This dual-criterion mechanism ensures that an engineering-compliant optimized design is reliably obtained at a minimal computational cost.

3.3. Algorithm Configuration and Evaluation Metrics

LHS is used to generate $N_{\text{init}} = 30$ initial sample points within the design space in the proposed SANOA-GP framework. Based on these samples, an initial GP surrogate model is constructed. An LCB acquisition function is used to prescreen candidate solutions during the subsequent virtual evolution phase, and its weight coefficient is set to $\kappa = 2.0$. When parameterization is applied, the exploitation of the predictive mean and exploration of the predictive variance are dynamically balanced.

DE, PSO, and SADEA are selected as comparative baselines to rigorously evaluate the algorithm performance. The population sizes across all comparative algorithms are uniformly set to $N_{\text{pop}} = 30$ to ensure equitable comparisons. Furthermore, the maximum computational budget is strictly capped at 150 full-wave EM simulations.

The prediction accuracy of the surrogate model under sparse data must be systematically verified to ensure reliable guidance during the search. An independent benchmark dataset containing 100 LHS samples is constructed for this purpose. Subsequently, true high-fidelity EM responses are extracted via full-wave electromagnetic simulations. The dataset is randomly partitioned into a training set of 80 samples and a test set of 20 samples. Four statistical metrics are used to objectively quantify the generalization performance: root mean square error (RMSE), mean absolute error (MAE), mean absolute percentage error (MAPE), and coefficient of determination (R^2).

To validate the superiority of the proposed GP-Matérn 5/2 model in handling non-smooth EM responses, three representative regression algorithms are selected as comparative baselines. A GP model based on the squared exponential kernel (GP-RBF) is introduced to evaluate the effectiveness of different kernels in capturing the abrupt spectral transitions of S_{11}. Additionally, Support Vector Regression (SVR) [21] and random forest [22] are incorporated, representing conventional kernel and ensemble learning methods, respectively. These two models are used to assess the generalization differences under a severely constrained dataset of only 80 training samples. All comparative models are finally trained and evaluated on identical datasets to ensure a rigorously equitable analysis.

4. RESULTS AND DISCUSSION

4.1. Surrogate Model Performance Validation

The statistical evaluation results of the various surrogate models on the test set are summarized in Table 2. The proposed GP (Matérn 5/2) and random forest models demonstrate comparable learning capabilities under sparse data conditions. Superior fitting accuracy is achieved for both models across the coefficient of determination (R^2), RMSE, and MAE. The GP (Matérn 5/2) demonstrates superior performance compared to the GP-RBF model ($R^2 = 0.452$). The substantial disparity confirms that the finite smoothness assumption of the Matérn

TABLE 2. Predictive performance comparison of different surrogate models on the test set.

Model	RMSE	MAE	MAPE (%)	R^2
GP (Matérn 5/2)	14.15	12.80	13.50	0.585
Random Forest	13.86	12.46	13.29	0.609
GP (RBF)	16.50	14.20	15.10	0.452
SVR	17.46	14.06	15.17	0.379

kernel aligns with the abrupt spectral transitions at the antenna's resonant frequencies. The overly smooth RBF kernel, in contrast, filters out crucial high-frequency details.

The SANOA framework ultimately adopts the GP (Matérn 5/2) as its core surrogate engine, although the random forest model maintains a marginal advantage in absolute prediction accuracy. The choice of GP is dictated by the LCB prescreening strategy, which relies on analytical predictive variance to balance exploration and exploitation dynamically. The random forest model does not inherently provide an analytical posterior variance due to its ensemble learning nature. The SVR model obtains the poorest overall metrics ($R^2 = 0.379$), revealing significant generalization deficiencies under severely constrained sample sizes. The GP (Matérn 5/2) maintains high predictive accuracy and provides indispensable uncertainty quantification. Therefore, the GP model achieves an optimal balance between accuracy and algorithmic functionality.

Figure 5 presents scatter plots of predicted fitness values against ground-truth values for the test set, with regression lines overlaid to evaluate fitting characteristics of each model. Highly similar scatter distributions are shown by the GP (Matérn 5/2) and random forest models, as depicted in Figs. 5(a) and (d). The predictions for both models are tightly clustered along the ideal diagonal, indicating negligible systematic bias and directly confirming their comparable statistical performance. The above result demonstrates that the GP model does not sacrifice regression accuracy despite its emphasis on probabilistic inference characteristics.

In contrast, Figs. 5(b) and (c) reveal a pronounced dispersion in the scatter plots for the GP (RBF) and SVR models, respectively. In particular, substantial deviations between the predictions and ground-truth values occur in low-fitness regions, which correspond to poor S_{11} performance. Introducing such pronounced modeling errors during optimization can easily mislead the search trajectory and degrade the global search efficiency. These visual results further confirm that the GP (Matérn 5/2) model can construct a high-fidelity virtual fitness landscape. Furthermore, these robust predictive capabilities enable effective global navigation of the complex, high-dimensional parameter space using the SANOA framework.

4.2. Optimization Efficiency and Convergence Analysis

This section systematically benchmarks the SANOA-GP against conventional swarm intelligence algorithms (Standard NOA, PSO, WOA [23], GWO [24]), classical surrogate-assisted algorithms (EGO, SADE, SAPSO [25], Offline-GP), and other advanced metaheuristic algorithms (BKA [26],

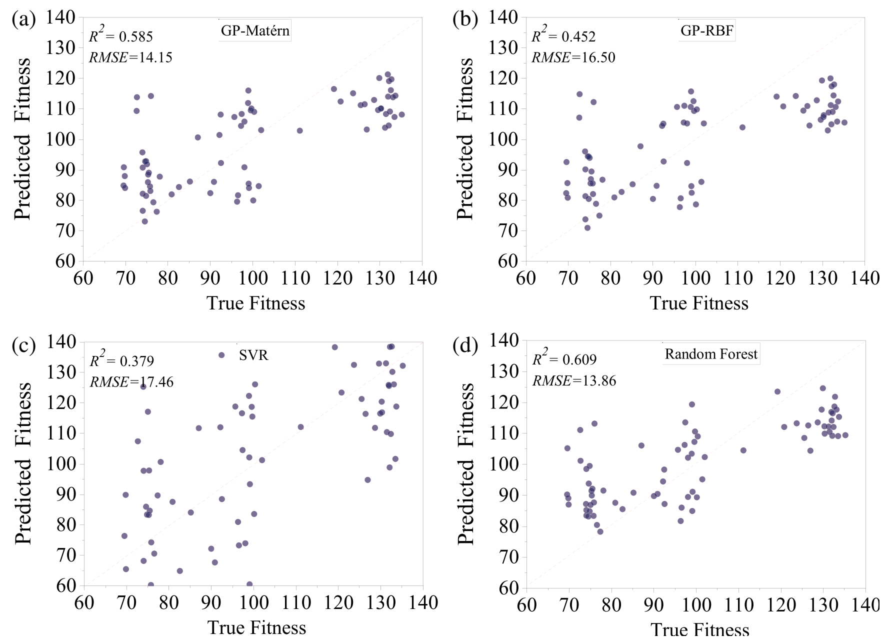

FIGURE 5. Regression scatter plots of predicted versus true fitness values on the test set for different surrogate models.

RIME [27]) on high-dimensional complex electromagnetic optimization problems. The performance-driven early stopping mechanism is temporarily disabled in the comparative study to allow objective observation of each algorithm's convergence limits and steady-state behavior. All algorithms are forced to run for the full computational budget of 150 full-wave EM simulations.

Figure 6 presents the best-so-far convergence trajectories from multiple independent trials (Best Run) to fairly compare the ultimate optimization potential of each algorithm, as metaheuristic algorithms are inherently stochastic. As observed, the SANOA-GP exhibits an explosive initial ascent. The algorithm breaches the 130-point target threshold within the first 10 simulations and ultimately stabilizes at a high fitness value of 137. The GP surrogate model and the lower confidence bound acquisition function provide an effective balance between global exploration and local exploitation, resulting in rapid convergence.

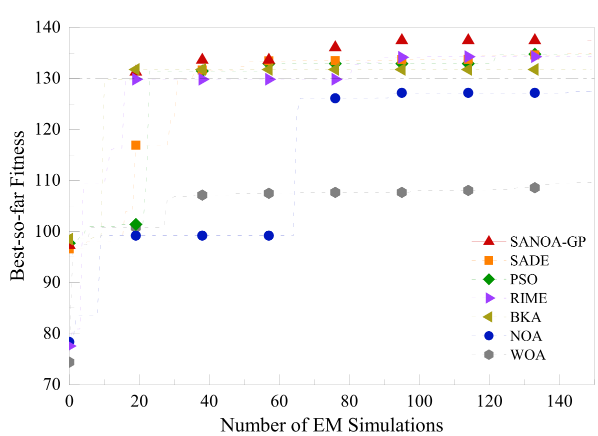

FIGURE 6. Convergence trajectories of the best-so-far fitness for different optimization algorithms.

In contrast, while the BKA demonstrates a highly competitive initial search speed, it stagnates without achieving higher breakthroughs in subsequent iterations. Standard PSO, SADE, and RIME eventually surpass the target threshold. However, their trajectories exhibit pronounced stepwise stagnation, and their final accuracies remain inferior to that of the SANOA-GP. Furthermore, standard NOA and WOA display severe stagnation throughout the entire iterative process, failing to reach the target threshold even after exhausting the simulation budget. The stark contrast reveals that metaheuristic search mechanisms alone are highly inefficient for navigating the complex, multimodal parameter space of dual-notch antennas.

To mitigate the stochasticity inherent in single-run evaluations, the statistical results obtained with the dual-termination criterion activated are summarized in Table 3. The results enable an objective assessment of each algorithm's practical engineering efficacy. Among all tested methods, SANOA-GP achieves the highest peak fitness (137.12) and mean fitness (131.84). In contrast, the surrogate-free standard NOA and WOA algorithms yield mean scores of merely 115.20 and 95.40, respectively. Such a marked performance gap confirms the necessity of surrogate-assisted strategies for overcoming high-dimensional multimodal traps. Notably, the SANOA-GP maintains clear superiority in both solution quality and stability, even when benchmarked against the highly competitive EGO algorithm (mean score: 130.50). The remaining algorithms generally fail to achieve a mean fitness above the 130-point threshold, indicating their vulnerability to local optima in complex electromagnetic landscapes.

Thanks to its performance-driven early stopping mechanism, the SANOA-GP requires an average of only 69.3 full-wave EM simulations (approximately 3.47 hours). Thus, the SANOA-GP robustly delivers a high-quality design while consuming less than half of the maximum computational budget. The BKA

TABLE 3. Performance and efficiency comparison of different optimization algorithms under the early stopping mechanism.

Algorithm	Best Fitness	Mean Fitness	Avg. Sims	Total Time (h)
SANOA-GP	**137.12**	**131.84**	69.3	3.47
EGO	136.51	130.50	75.0	3.75
PSO	134.50	128.42	85.4	4.27
RIME	134.26	127.93	76.5	3.83
SADE	133.80	128.10	92.1	4.60
BKA	131.76	126.76	**65.9**	**3.30**
SAPSO	130.19	124.30	79.7	3.99
Offline-GP	128.40	118.20	150.0	≥ 7.50
NOA	127.38	115.20	150.0	≥ 7.50
GWO	126.50	110.50	150.0	≥ 7.50
WOA	109.66	95.40	150.0	≥ 7.50

TABLE 4. Design variables and their optimal values.

Parameter	L_1	W_1	T_1	T_2	T_3	U_1	U_2	U_3	d	c
Optimal Value (mm)	8.24	7.18	6.33	1	1.29	3.81	4.75	3.77	0.34	0.78

achieves a nominally lower average simulation count (65.9) but only an inadequate mean fitness (126.76), indicating that the algorithm easily gets trapped in local optima. On the other hand, although PSO and SADE can converge in their best single runs, their average simulation counts reach as high as 85.4 and 92.1, respectively, indicating that their rapid convergence is highly stochastic and heavily dependent on initial sampling. The above comprehensive comparison strongly demonstrates that the SANOA-GP drastically shortens the development cycle while consistently ensuring high optimization accuracy.

4.3. Ablation Study on Acquisition Function

In this section, an ablation study is conducted on the core confidence-bound prescreening strategy to elucidate the optimization mechanism of the SANOA-GP framework under sparse-data conditions. Three acquisition function configurations are compared: a pure exploitation strategy relying exclusively on the predictive mean (Mean-Only), a pure exploration strategy driven solely by the predictive variance (Variance-Only), and the proposed dynamic balance strategy ($\mu + 2.0\sigma$).

Figure 7 illustrates the convergence trajectories of the best fitness scores for the three strategies under a budget of 150 cycles. The Mean-Only strategy (blue line) rapidly stagnates near a fitness of 120 early in the optimization. When guided exclusively by the predictive mean, the optimization process is easily misled by the biases of the initial surrogate model, thereby completely losing the ability to escape the local optima. In contrast, the Variance-Only strategy (green line) achieves a rapid initial ascent by aggressively exploring uncharted design boundaries. However, the variance-only strategy is completely deprived of mean-driven guidance. Once reaching a fitness of 131, the strategy loses the precision to fine-tune within local neighborhoods. It thus ceases to improve further.

In stark contrast, the proposed $\mu + 2.0\sigma$ strategy (red line) demonstrates superior robustness and optimization depth. By judiciously integrating variance compensation, this strategy dynamically balances the exploration of highly uncertain regions with the exploitation of known high-performing areas. Consequently, the algorithm not only robustly surpasses the 130-point target threshold but also ultimately surges to a peak fitness of approximately 137. The comparative findings mechanistically confirm that both mean-driven exploitation and variance-driven exploration are indispensable. Therefore, the synergistic integration of both mechanisms is imperative for achieving efficient global convergence over computationally expensive multimodal design spaces.

4.4. Antenna Physical Response and Mechanisms

The physical viability of the optimization results is verified by the optimal design parameters and corresponding simulated S_{11} spectral response. The complete set of parameters is listed in Table 4, including the angular values $R_1 = 9°$ and $R_2 = 2.63°$. The S_{11} response is illustrated in Fig. 8. The optimized antenna achieves broadband impedance matching outside the designated notch bands across the 3.1–10.6 GHz spectrum, with passband $S_{11} < -10$ dB. More importantly, the antenna creates two highly selective deep notches precisely at the target interference frequency.

Figure 8 explicitly delineates the stopband bandwidths at the -5 dB threshold. The lower-frequency notch spans 4.51–4.66 GHz, thereby precisely suppressing the 5G N79 signal. The higher-frequency notch covers 7.31–7.65 GHz, thereby shielding the receiver from X-band interference. S_{11} peaks approach 0 dB at both notch centers. Such profound rejection significantly surpasses the initial -5 dB design metric, thereby guaranteeing high-performance filtration. The observed phys-

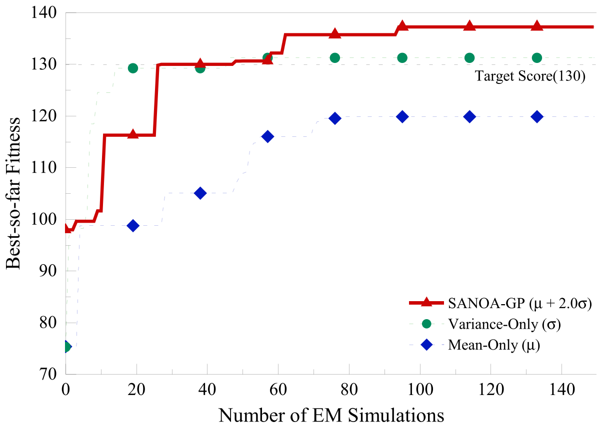

FIGURE 7. Ablation study of different acquisition function strategies.

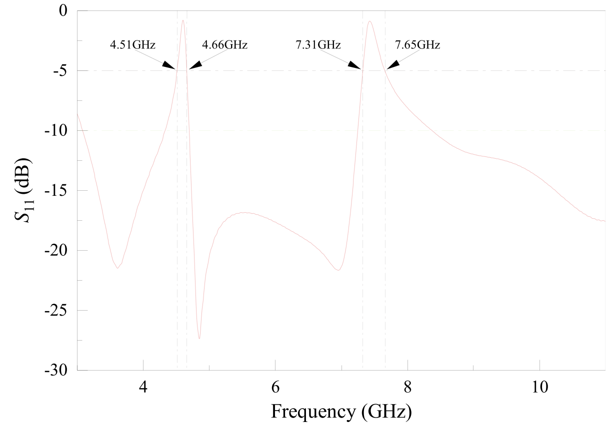

FIGURE 8. Simulated S_{11} spectral response of the optimal dual-notched antenna obtained by SANOA-GP.

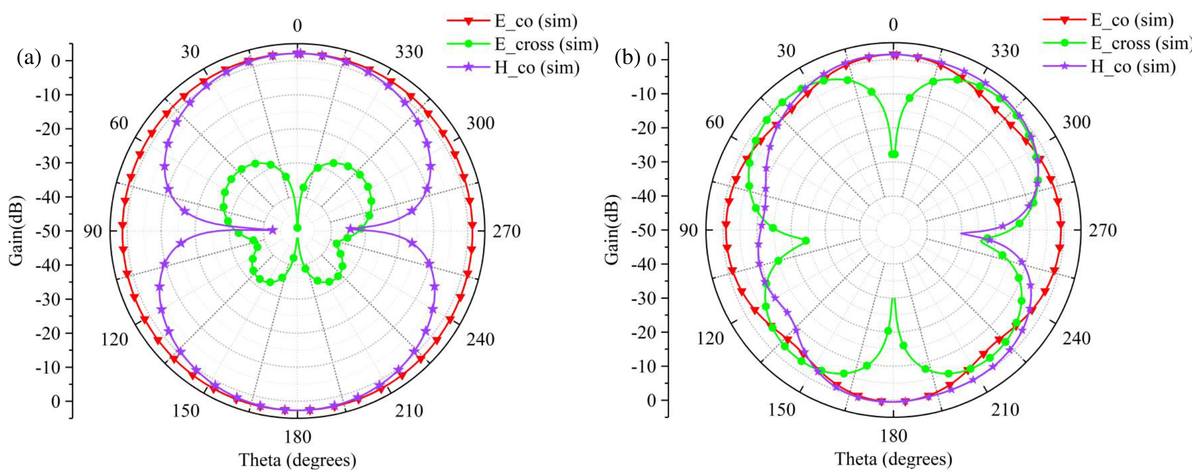

FIGURE 9. Simulated 2D radiation patterns of the optimized antenna at 3.6 GHz and 10.0 GHz.

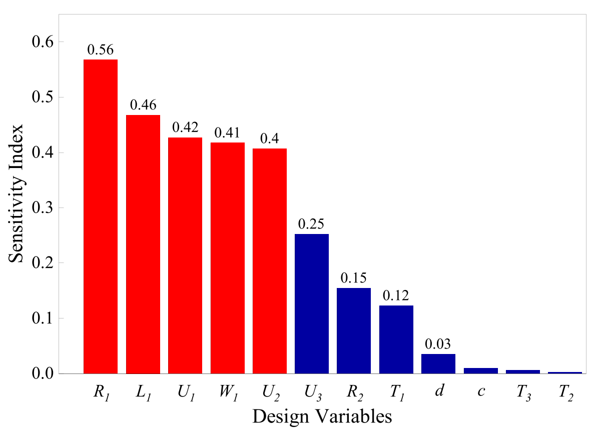

FIGURE 10. Bar chart of the Sobol total-effect sensitivity indices for the design variables.

ical responses confirmed the reliability of numerical optimization. The strong agreement between the measurements and simulations further validates the SANOA-GP framework. The framework effectively navigates highly sensitive, multimodal landscapes in high-dimensional parameter spaces.

In addition to frequency-domain impedance matching, spatial radiation stability is an important metric for evaluating UWB antenna performance. For a comprehensive assessment of the far-field radiation characteristics of the optimized antenna, Figs. 9(a) and (b) present the simulated 2D radiation patterns at 3.6 and 10.0 GHz, respectively. The frequencies are chosen outside the notched bands to reflect the spatial radiation features during normal communication.

As observed at 3.6 GHz, the antenna exhibits the typical radiation properties of a standard planar monopole. The E-plane pattern is a symmetric figure-of-eight, and the H-plane pattern is stable and omnidirectional. Such radiation properties provide uniform signal coverage for broadband wireless systems. As the operating frequency increases to 10.0 GHz, the electrical dimensions of the radiator expand significantly relative to the wavelength, causing higher-order modes to excite on the radiating surface. This results in a slight distortion of the E-plane pattern and an elevated cross-polarization level. However, in the principal radiation directions, namely the broadside directions at $\theta = 0°$ and $180°$, the cross-polarization level remains over 20 dB below the co-polarization level. This phenomenon is inherent to UWB antennas. Nevertheless, the antenna maintains a

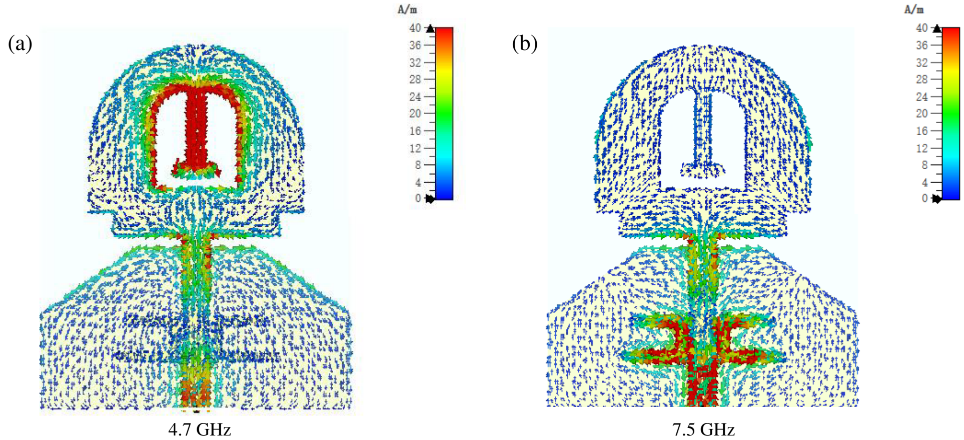

FIGURE 11. Simulated surface current distributions of the optimized antenna at the two notch center frequencies.

robust overall radiation performance across the high-frequency band. In the H-plane, the cross-polarization components remain at an extremely low level across the entire operating band and are therefore invisible in the plotted patterns. Such suppression originates from the strict geometric symmetry of the planar monopole along the feeding axis. The symmetry inherently forces the orthogonally polarized electric fields to mutually cancel out in the far-field region.

4.5. Key Parameter Sensitivity Analysis and Physical Mechanisms

A multi-dimensional theoretical cross-validation of the optimization results is conducted using Sobol global sensitivity analysis and surface current distributions. The analysis elucidates the physical mechanisms underlying the dual-notch characteristics.

Figure 10 presents Sobol total-effect sensitivity indices in design variables, derived from the SANOA-GP surrogate model. The statistical results show that arc R_1 of the inverted T-shaped stub and slot height L_1 of the semi-circular slots exhibit the highest sensitivities, with total-effect indices exceeding 0.45. As the primary determinants of the 4.7 GHz lower-frequency notch, even minor perturbations in R_1 and L_1 can induce substantial fluctuations in the fitness functions. The dimensions of the parasitic stubs (U_1, W_1, and U_2) show the next highest sensitivities, primarily governing the electromagnetic response of the 7.5 GHz notch.

From an electromagnetic perspective, the extreme sensitivities of R_1 and L_1 arise from their direct control over the effective electrical length of the inverted T-shaped stub and semi-circular slots. According to transmission line theory, the resonant frequency of a notch structure is inversely proportional to its effective electrical length. Consequently, even submillimeter variations in the high-Q resonators lead to severe frequency shifts and abrupt S_{11} deteriorations, fundamentally explaining their highest sensitivity indices.

Figure 11 shows the simulated surface current distributions of the optimized antenna at the notch center frequencies. As shown in Fig. 11(a), the surface currents are highly concentrated along the edges of the inverted U-shaped slot at 4.7 GHz. The currents on the inner and outer boundaries flow in opposite directions, exhibiting pronounced antiparallel behavior. This antiparallel current distribution excites a strong localized resonance that effectively blocks far-field radiation, thereby explaining why R_1 and L_1 (dimensions governing the slot) are highly sensitive.

As shown in Fig. 11(b), the dominant current distribution shifts significantly to the parasitic stubs as the operating frequency increases to 7.5 GHz, where the stubs function as high-quality-factor band-stop filters. Driven by near-field electromagnetic coupling, the signal energy is reflected back to the excitation port rather than being radiated outward. This behavior aligns perfectly with the result in Fig. 10, where U_1 and W_1 dominate the higher-frequency response. The mutual corroboration between the Sobol sensitivity analysis and EM field distributions provides a strong physical explanation for the underlying mechanisms of the dual-notch responses.

4.6. Prototype Fabrication and Measurement Validation

A physical antenna prototype was fabricated using the optimized geometric parameters to comprehensively verify the effectiveness of the proposed design and SANOA-GP algorithm. The measured S_{11} curves are obtained using a vector network analyzer. Fig. 12 presents the measured curves, corresponding Computer Simulation Technology (CST) full-wave simulation results, and an inset photograph of the fabricated prototype.

Excellent agreement between the measured and simulated results is shown in Fig. 12. The measured impedance bandwidth successfully covered the target 3.1–10.6 GHz UWB range, and the two highly selective stopbands precisely matched the simulated 4.51–4.66 GHz and 7.31–7.65 GHz bands. The measured and simulated curves exhibited slight discrepancies in notch depths and minor resonant frequency shifts. The deviations mainly originate from three factors: manufacturing tolerances of the FR-4 substrate, parasitic electromagnetic effects of the SMA connector, and inherent losses in the testing environment and RF cables. Despite such fabrication and measurement tolerances, the overall spectral profiles maintained excellent con-

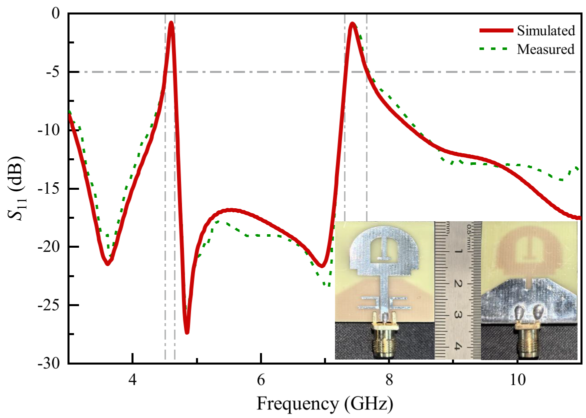

FIGURE 12. Photograph of the fabricated antenna prototype and comparison between the measured and simulated S_{11} results.

sistency. The measurement results confirmed that the fabricated antenna successfully achieved the expected dual-notch characteristics, thereby satisfying the operational requirements of complex EM environments. Experimental validation further confirmed the high predictive accuracy of the SANOA-GP framework and its practical engineering viability for solving high-dimensional antenna optimization problems.

5. CONCLUSION

A novel co-design framework based on SANOA-GP is proposed for the efficient automated design of UWB dual-band-notched antennas. The SANOA-GP framework integrates GP-based probabilistic prediction with an LCB acquisition function to accurately quantify epistemic uncertainty and intelligently balance exploration and exploitation across the non-convex, multimodal parameter space. Compared with conventional surrogate-free metaheuristic algorithms, such as PSO and Standard NOA, the proposed co-design framework incorporates a performance-driven dual-early-stopping mechanism. Consequently, it requires an average of only 69.3 full-wave EM simulations to attain the global optimum and reduce the time cost by over 50% while ensuring high optimization accuracy. Furthermore, Sobol global sensitivity analysis is incorporated to break the inherent uninterpretability of the black-box optimization. Surface current distributions are used to corroborate the underlying physical mechanisms. The measured results of the fabricated prototype show excellent agreement with the simulation predictions, demonstrating highly selective suppression of the 5G N79 and X-band. The proposed SANOA-GP framework establishes a high-precision and efficient computing paradigm with broad application prospects in complex RF engineering.

REFERENCES

[1] Sakkila, L., C. Tatkeu, A. Rivenq, J. Zaidouni, and M. Bocquet, "UWB radar detection theory," in *2020 10th International Symposium on Signal, Image, Video and Communications (ISIVC)*, 1–5, Saint-Etienne, France, 2021.

[2] Wang, X., S. Zhang, S. Chen, L. Hou, and L. Zhu, "An antijamming method based on multichannel singular spectrum analysis and affinity propagation for UWB ranging sensors," *IEEE Sensors Journal*, Vol. 23, No. 11, 11 869–11 878, Jun. 2023.

[3] Yadav, R. and L. Malviya, "UWB antenna and MIMO antennas with bandwidth, band-notched, and isolation properties for high-speed data rate wireless communication: A review," *International Journal of RF and Microwave Computer-Aided Engineering*, Vol. 30, No. 2, e22033, 2020.

[4] Singh, C., C. Sharma, and A. Kumar, "Miniaturized ultra-wideband microstrip antenna with triple band-notched characteristics at WiMAX/WLAN/X-band for medical applications," *Physica Scripta*, Vol. 100, No. 5, 055523, 2025.

[5] Pasumarthi, S. R., K. V. Babu, J. Kavitha, and U. Jayaram, "High performance triple band-notched UWB monopole antenna for mitigation of narrowband interference," *Physica Scripta*, Vol. 100, No. 7, 075567, Jul. 2025.

[6] Bouchachi, I., A. Reddaf, M. Boudjerda, K. Alhassoon, B. Babes, F. N. Alsunaydih, E. Ali, M. Alsharef, and F. Alsaleem, "Design and performances improvement of an UWB antenna with DGS structure using a Grey Wolf Optimization algorithm," *Heliyon*, Vol. 10, No. 5, e26337, Mar. 2024.

[7] Li, Y., W. Li, and R. Mittra, "A compact CPW-fed circular slot antenna with reconfigurable dual band-notch characteristics for UWB communication applications," *Microwave and Optical Technology Letters*, Vol. 56, No. 2, 465–468, Feb. 2014.

[8] Koziel, S. and A. Pietrenko-Dabrowska, "Global EM-driven optimization of multi-band antennas using knowledge-based inverse response-feature surrogates," *Knowledge-Based Systems*, Vol. 227, 107189, Sep. 2021.

[9] Storn, R. and K. Price, "Differential evolution — A simple and efficient heuristic for global optimization over continuous spaces," *Journal of Global Optimization*, Vol. 11, No. 4, 341–359, Dec. 1997.

[10] Wang, Z., N. Zhang, J. Huang, Y. Cui, W. Ren, H. Hou, J. Zhao, and K. Yu, "Design of multi-sense antenna with coupled lines based on cryptogenic particle swarm optimization," *IEEE Antennas and Wireless Propagation Letters*, Vol. 24, No. 11, 3946–3950, Nov. 2025.

[11] Güneş, F., S. Demirel, and S. Nesil, "A novel design approach to X-band Minkowski reflectarray antennas using the full-wave EM simulation-based complete neural model with a hybrid GA-NM algorithm," *Radioengineering*, Vol. 23, No. 1, 144–153, 2014.

[12] Dong, J., Y. Li, and M. Wang, "Fast multi-objective antenna optimization based on RBF neural network surrogate model optimized by improved PSO algorithm," *Applied Sciences*, Vol. 9, No. 13, 2589, 2019.

[13] Sendrea, R. E., C. L. Zekios, and S. V. Georgakopoulos, "A review of multi-fidelity learning approaches for electromagnetic problems," *Electronics*, Vol. 14, No. 1, 89, 2025.

[14] Rahman, M., D.-S. Ko, and J.-D. Park, "A compact multiple notched ultra-wide band antenna with an analysis of the CSRR-TO-CSRR coupling for portable UWB applications," *Sensors*, Vol. 17, No. 10, 2174, 2017.

[15] Yang, W., S. Liu, and J. Yang, "An optimized surrogate model and algorithm with rapid multi-parameter processing capability for antenna design," *Measurement*, Vol. 241, 115719, Feb. 2025.

[16] Gao, J., Y. Tian, and X. Chen, "Antenna optimization based on co-training algorithm of Gaussian process and support vector machine," *IEEE Access*, Vol. 8, 211 380–211 390, 2020.

[17] Abdel-Basset, M., R. Mohamed, M. Jameel, and M. Abouhawwash, "Nutcracker optimizer: A novel nature-inspired metaheuristic algorithm for global optimization and engineering design problems," *Knowledge-Based Systems*, Vol. 262, 110248, Feb. 2023.

[18] Manfredi, P., "Probabilistic uncertainty propagation using gaussian process surrogates," *International Journal for Uncertainty Quantification*, Vol. 14, No. 6, 71–104, 2024.

[19] Jones, D. R., M. Schonlau, and W. J. Welch, "Efficient global optimization of expensive black-box functions," *Journal of Global Optimization*, Vol. 13, No. 4, 455–492, Dec. 1998.

[20] Koziel, S. and A. Pietrenko-Dabrowska, "Efficient simulation-based global antenna optimization using characteristic point method and nature-inspired metaheuristics," *IEEE Transactions on Antennas and Propagation*, Vol. 72, No. 4, 3706–3717, Apr. 2024.

[21] Zhang, F. and L. J. O'Donnell, "Support vector regression," in *Machine Learning: Methods and Applications to Brain Disorders*, 123–140, Cambridge, MA, USA, 2020.

[22] Breiman, L., "Random forests," *Machine Learning*, Vol. 45, No. 1, 5–32, Oct. 2001.

[23] Mirjalili, S. and A. Lewis, "The whale optimization algorithm," *Advances in Engineering Software*, Vol. 95, 51–67, May 2016.

[24] Mirjalili, S., S. M. Mirjalili, and A. Lewis, "Grey Wolf Optimizer," *Advances in Engineering Software*, Vol. 69, 46–61, Mar. 2014.

[25] Harrison, K. R., A. P. Engelbrecht, and B. M. Ombuki-Berman, "Self-adaptive particle swarm optimization: A review and analysis of convergence," *Swarm Intelligence*, Vol. 12, No. 3, 187–226, 2018.

[26] Wang, J., W.-C. Wang, X.-X. Hu, L. Qiu, and H.-F. Zang, "Black-winged kite algorithm: A nature-inspired meta-heuristic for solving benchmark functions and engineering problems," *Artificial Intelligence Review*, Vol. 57, No. 4, 98, 2024.

[27] Su, H., D. Zhao, A. A. Heidari, L. Liu, X. Zhang, M. Mafarja, and H. Chen, "RIME: A physics-based optimization," *Neurocomputing*, Vol. 532, 183–214, 2023.